Supplementary Information

Initiating a composite membrane with localized high iodine concentration layer based on adduct chemistry to enable highly reversible zinc-iodine flow batteries

Yichan Hu,[†abc] Tao Hu,[†a] Yuanwei Zhang,[d] Haichao Huang,[d] Yixian Pei,[d] Yihan Yang,[e] Yudong Wu,[a] Haibo Hu,*[a] Guojin Liang,*[bd] and Hui-Ming Cheng[bd]

[a]School of Materials Science and Engineering, Anhui University, Hefei 230601, China.
[b]Faculty of Materials Science and Energy Engineering, Shenzhen University of Advanced Technology, Shenzhen 518055, China.
[c]School of Materials Science and Engineering, Hunan University, Changsha 410000, China.
[d]Institute of Technology for Carbon Neutrality, Shenzhen Institute of Advanced Technology, Chinese Academy of Sciences (CAS), Shenzhen 518055, China.
[e]School of Physics and Electronics, Hunan University, Changsha 410000, China.

Email: haibohu@ahu.edu.cn; gj.liang@siat.ac.cn

†These authors contributed equally.

Experimental Section

Materials:

Zn and Ti foil (0.2 mm) are bought from Shengshida Metal Material Co.Ltd. (Dongguan, China). Graphite felt (3.0 mm, carbon≥99 %, bulk density 0.12-0.14 g cm^{-2}) was received from Yi Deshang Carbon Technology. $ZnBr_2$, ZnI, I_2, KI, KCl, and NMP of analytical purity are bought from Aladdin Reagent Co. Ltd. (Shanghai, China). Al_2O_3, TiO_2, ZrO_2, CeO_2, and MgO (particle size 50 nm, 99.9 % metals basis) were purchased from Microline Co. Ltd. (Shanghai, China). PVDF (HSV900) binder was purchased from Taiyuan Lizhiyuan battery. The porous polyolefin membrane was purchased from Wuhan Zhisheng.

Preparation of electrolytes:

Posolyte consisting of 1 M ZnI_2 was prepared by dissolving 1.436 g of ZnI_2 in 4.5 ml deionized water. Negolyte consisting of 1 M $ZnBr_2$ and 1 M KCl was prepared by dissolving 1.01 g of $ZnBr_2$ and 0.335 g of KCl in 4.5 ml deionized water.

Preparation of localized high iodine concentration (LHIC) composite membranes:

Porous polyolefin membranes were purchased without any further treatment. The membrane was cut into a square with a size of 2*2 cm^{-2}. The LHIC composite membranes were prepared by casting slurry with Oxide: PVDF: NMP = 8:1:1. The slurry volume regulates the oxide loading on the positive side of the porous polyolefin film. The poured membrane is then dried in an oven at 60°C overnight.

Permeability:

The permeability of KI_x through LHIC membranes was determined from the evolution of the UV-visible spectra of the permeate side in H-cell tests (**Figure S9**). The feed reservoir was filled with 1 M KI_x, while the permeate side was filled with deionized water. The two pools had a circularly symmetrical transport channel separated by a porous polyolefin/LHIC membrane. It was assumed that the change of KI_x concentration in the feed solution reservoir was negligible when their concentration on the permeation side was low, and the flux of KI_3 through the membrane is a constant; that is, a pseudo-steady-state condition prevails in the two reservoirs during experiments[1,2].

$$V_B \frac{dc_B(t)}{dt} = \frac{AP}{L} [C_A - C_B(t)]$$

$$ln\left(1-\frac{C_B(t)}{C_A}\right)=-\frac{AP}{LV_B}\left[t-t_0\right]$$

where C_A and $C_B(t)$ are the concentrations (mol L^{-1}) of KI_3 in the feed and permeate side, respectively. A and L are the area (cm^2) and thickness (cm) of the membrane, respectively. V is the volume of the permeate solution (ml); P is the membrane permeability (cm^2 min^{-1}), t is the time (min), and t_0 is the time lag (min). The permeability P could be determined from the slope of the plot of $-\ln(1-c_B(t)/c_A)$ versus t.

ZIFB battery assembly:

First, a polytetrafluoroethylene (PTFE) frame was used as a flow channel to fix the position of a carbon felt electrode with a geometric area of 4.0 cm^2 (2.0 × 2.0 cm^2) and a thickness of 3.0 mm. The graphite plate is a current collector for positive and negative electrodes. A peristaltic pump is used to power the electrolyte flow through the electrode to manufacture flow-mode batteries.

Electrochemical characterization:

The EIS test was conducted on the CHI electrochemical test device (760E, CH Instruments, Inc.). Drift-diffusion measurements were made by self-made double-chamber diffusion cells. Two compartments filled with different concentrations of potassium chloride solution and connected with a pair of Ag/AgCl salt bridge electrodes were applied with CHI 760E voltage from -25mV to 25mV, recording the current. The constant current characteristics of ZIFB cells were tested on a battery test system (LAND, CT2001A) at room temperature (unless otherwise specified) or high temperature (60 °C) in an incubator. The charging process is limited by a constant capacity (10 mAh cm^{-2} or 20 mAh cm^{-2}), and a cut-off voltage of 0.01 V determines the discharge process. In the discharge program, after the initial discharge is discharged at the charge current magnitude, the remaining charge is removed at 1/4 the discharge current. The theoretical capacity is calculated by posolyte (iodide part), which is the capacity-limiting side of the whole battery.

Material characterization:

The morphology and chemical composition of all the samples are analyzed by scanning electron microscopy (S-4800, Hitachi, Japan) and X-ray diffraction spectra (Bruker d8 advanced Kα-ray diffractometer (λ=1.54056 Å). The concentration of the permeate side was tested by an ultraviolet-visible spectrophotometer (Lambda 365,

PerkinElmer). The water contact angle of the film sample was measured on JC2000D1 (Shanghai Zhongchen Digital Technology Equipment Co., Ltd., China). The fixed droplet method was used at room temperature. A microsyringe places a deionized water droplet on a membrane surface in the air. After 10 s, the image of the droplet is recorded, and the contact angle of the water is measured from the recorded image.

Molecular dynamics (MD) calculation:

The molecular configurations and binding energies between various carbon spheres and phosphorus were calculated using density functional theory within the Dmol3 package [3,4] The generalized gradient approximation (GGA) and Perdew-Burke-Ernzerhof (PBE) functional were used for the exchange-correlation energy and correlation interaction calculations. The convergence criteria applied for Dmol3 geometry optimizations were 0.002 Ha·Å^{-1}, 0.005 Å, and 1.0 × 10^{-5} Ha for the maximum force, maximum displacement, and energy change, respectively. The binding energy (Eb) between carbon spheres and phosphorus is defined as follows:

$$E_b = E_{I_x^-@oxide} - E_{I_x^-} - E_{oxide}$$

where $E_{I_x^-@oxide}$, $E_{I_x^-}$, and E_{oxide} are total energies of I_x^-@oxide, I_x^-, and oxide, respectively.

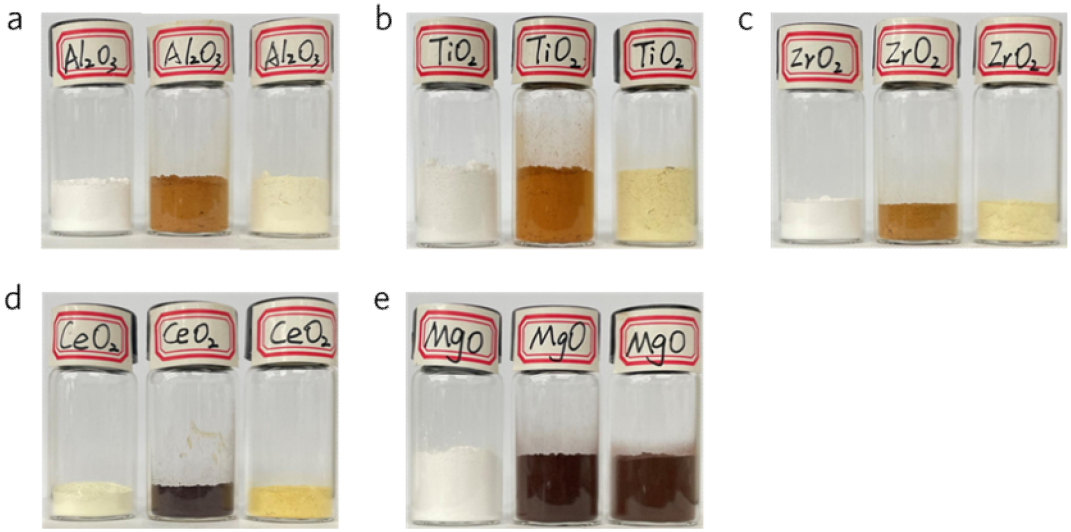

Figure S1. Optical photos of different oxides dried in a 70 °C oven at different durations, each group of pictures from left to right is the initial oxides, iodine-oxide adducts of dried 12 h and dried 72 h, respectively.

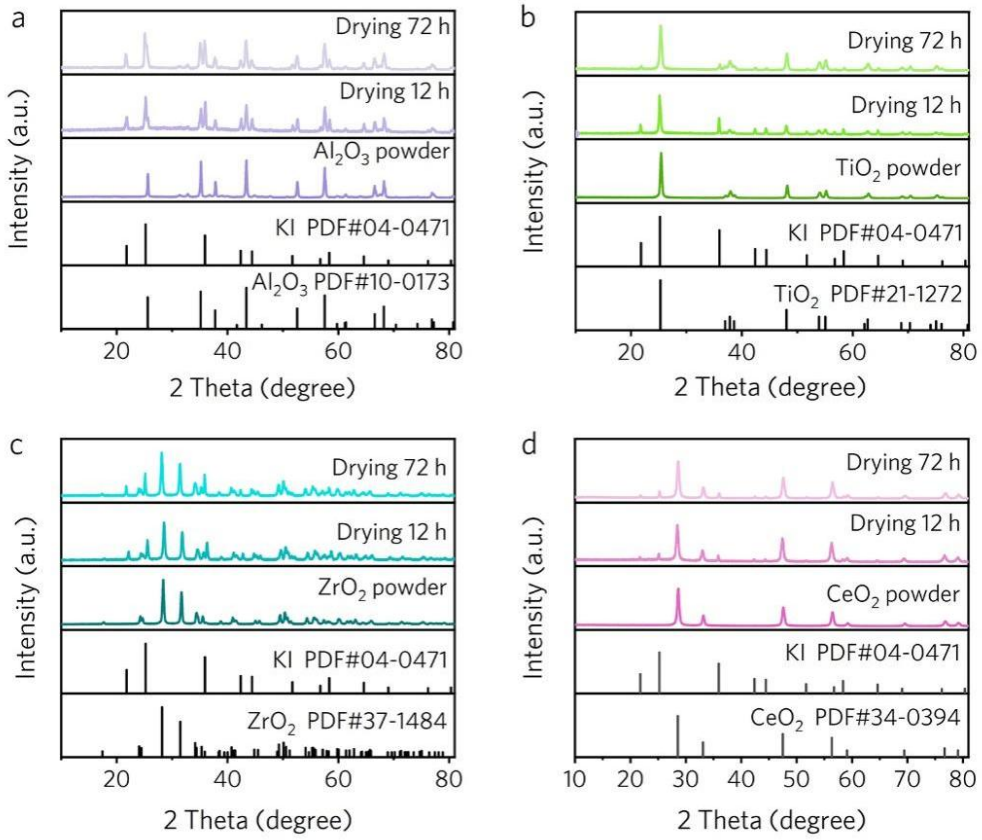

Figure S2. The XRD profiles of different oxide-based adducts were placed in a 70 °C oven in different states: a) Al_2O_3, b) TiO_2, c) ZrO_2, and d) CeO_2.

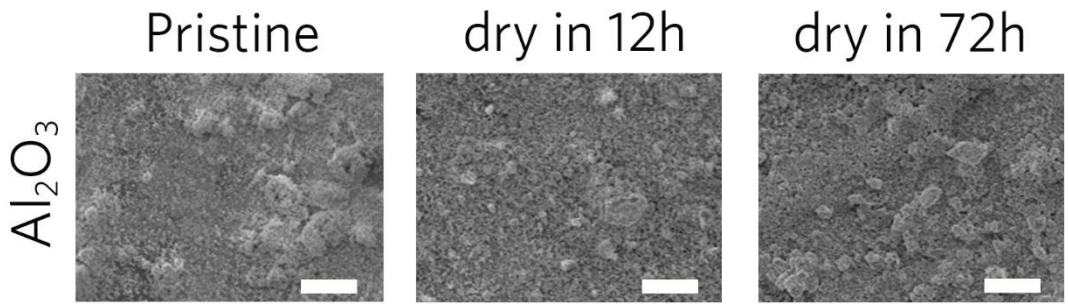

Figure S3. SEM images of Al_2O_3 dried at different durations in a 70 °C oven, scale bar: 60um.

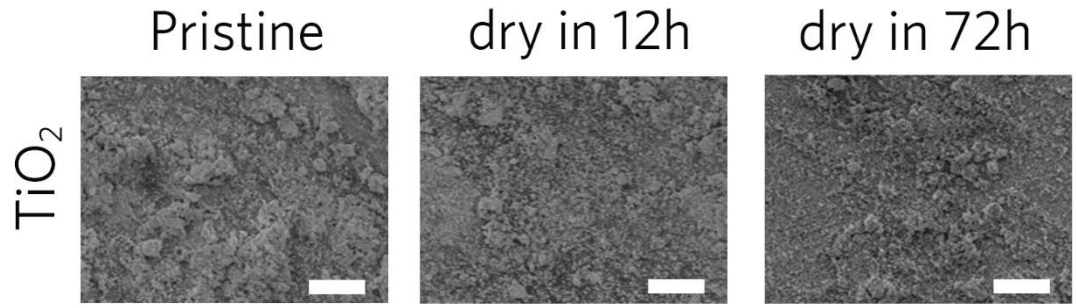

Figure S4. SEM images of TiO_2 dried at different durations in a 70 °C oven, scale bar: 60um.

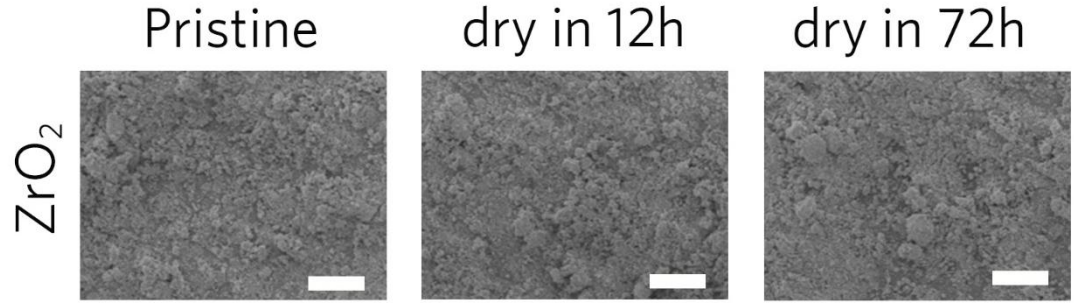

Figure S5. SEM images of ZrO_2 dried at different durations in a 70 °C oven scale bar: 60um.

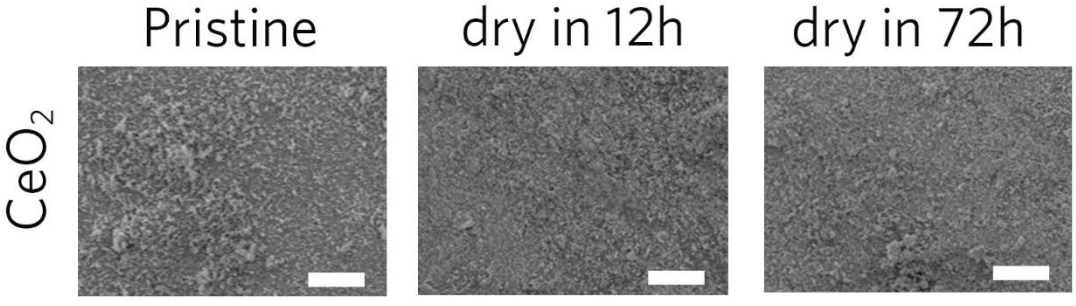

Figure S6. SEM images of CeO_2 dried at different durations in a 70 °C oven scale bar: 60um.

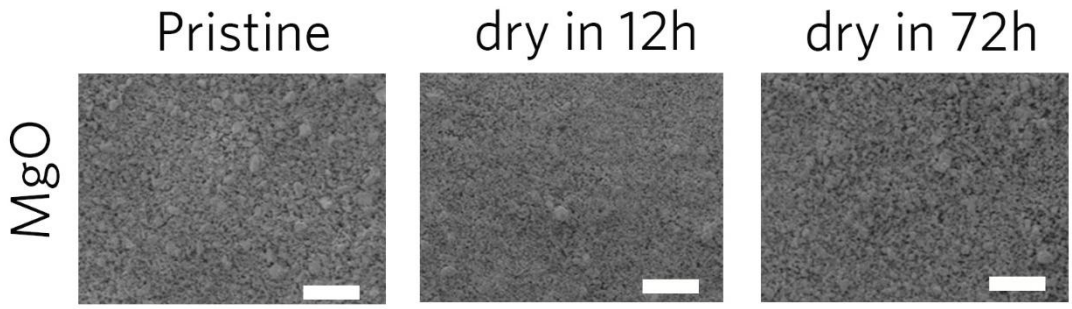

Figure S7. SEM images of MgO dried at different durations in a 70 °C oven scale bar: 60um.

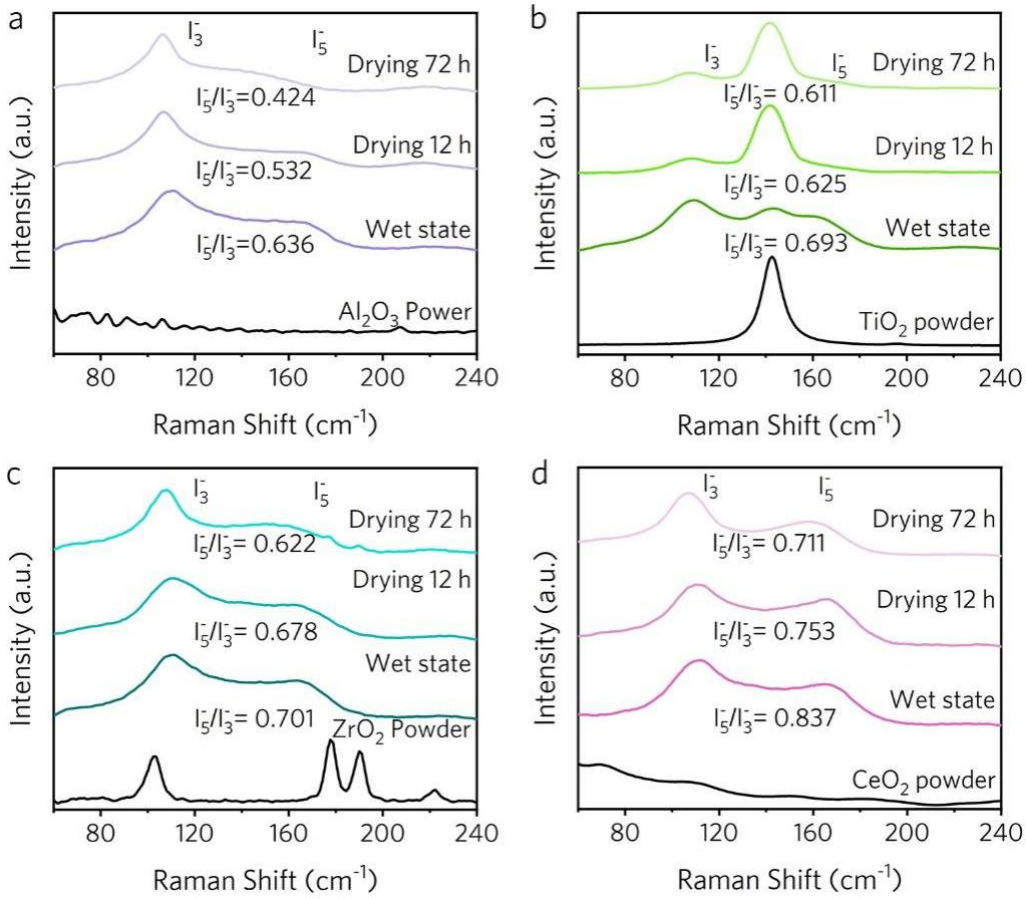

Figure S8. The Raman spectra of different oxides in different states: a) Al_2O_3, b) TiO_2, c) ZrO_2, d) CeO_2.

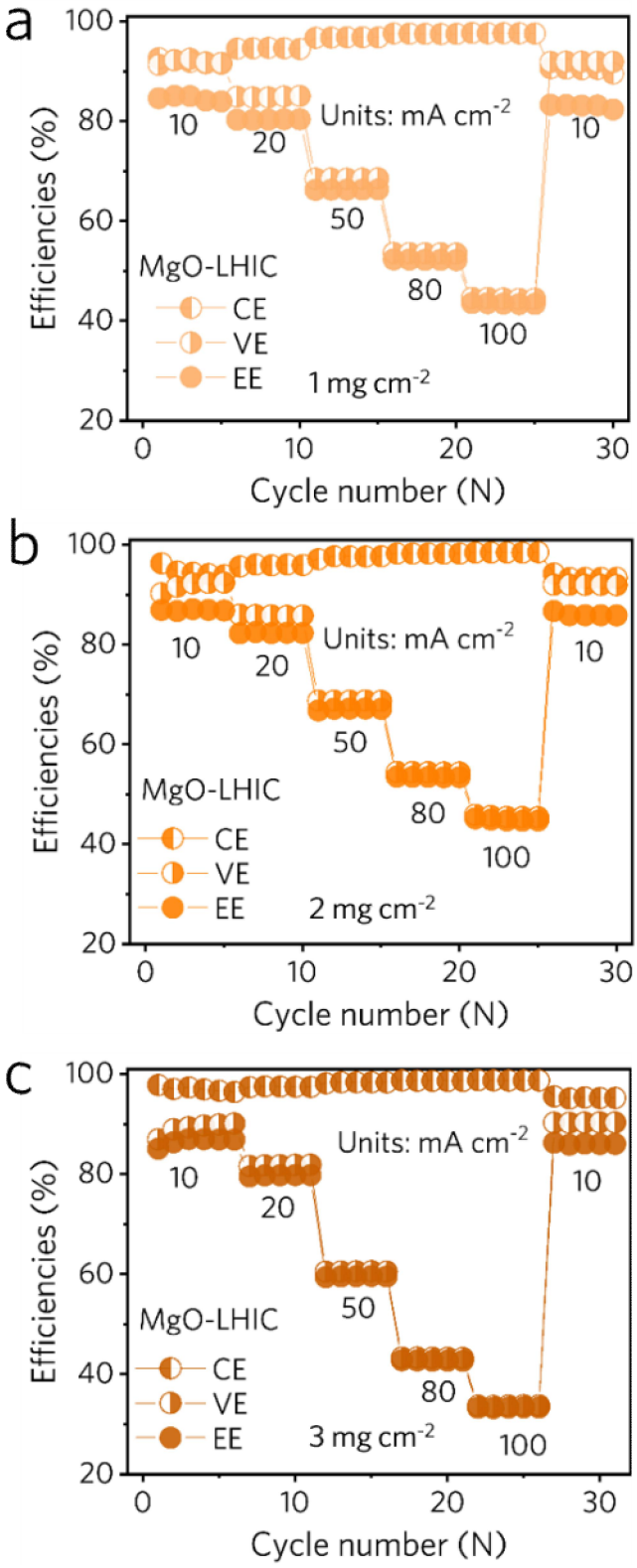

Figure S9. The rate performance of LHIC-based batteries was based on different adduct loading contents in 60 °C: a) 1 mg cm^{-2}, b) 2 mg cm^{-2}, c) 3 mg cm^{-2}.

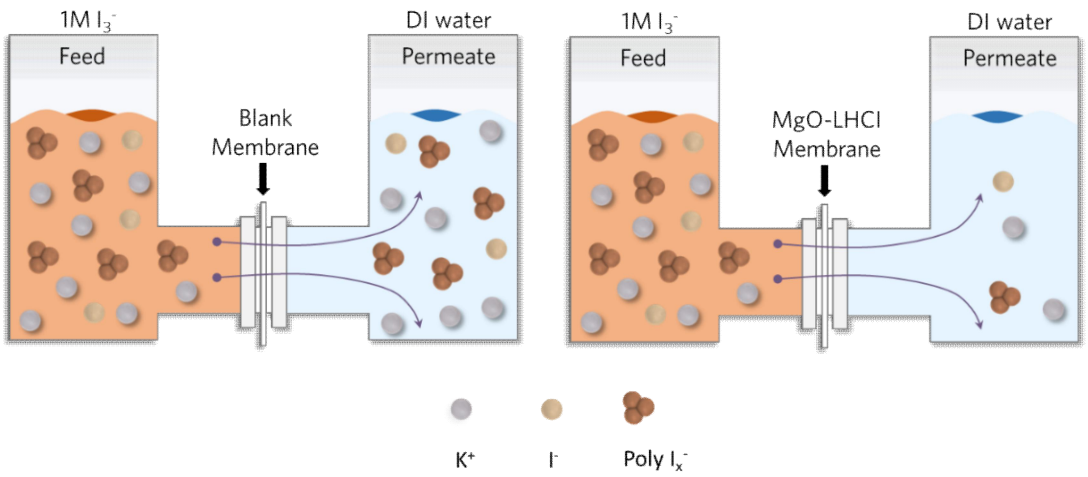

Figure S10. Schematic of ion permeation measurements. Two-compartment H-cell testing configuration of 1 M KI_x permeation using (a) Blank membrane and (b) MgO-LHIC membrane.

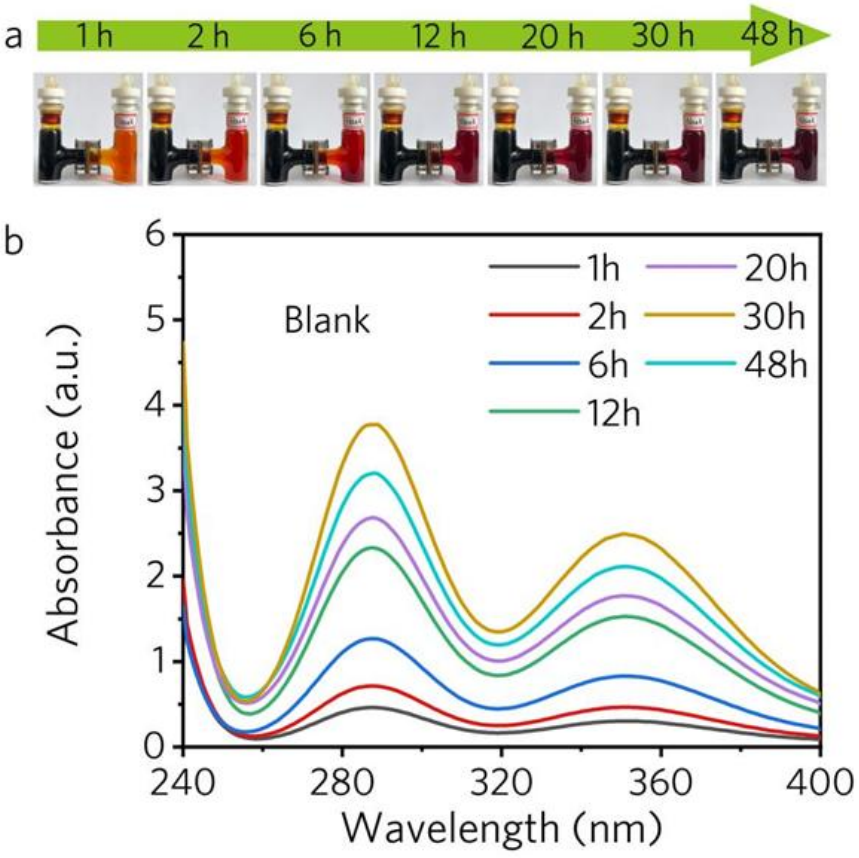

Figure S11. Porous polyolefin membrane penetration experiment in different durations: a) Optical photos and b) UV-vis results of the KI_x permeate side.

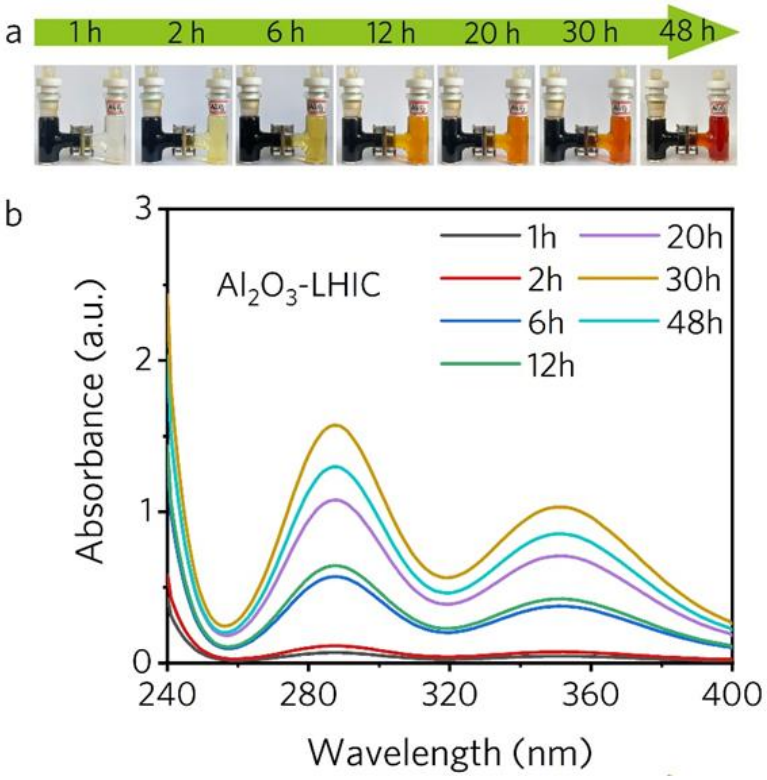

Figure S12. Al_2O_3-LHIC membrane penetration experiment in different durations: a) Optical photos and b) UV-vis results of the KI_x permeate side.

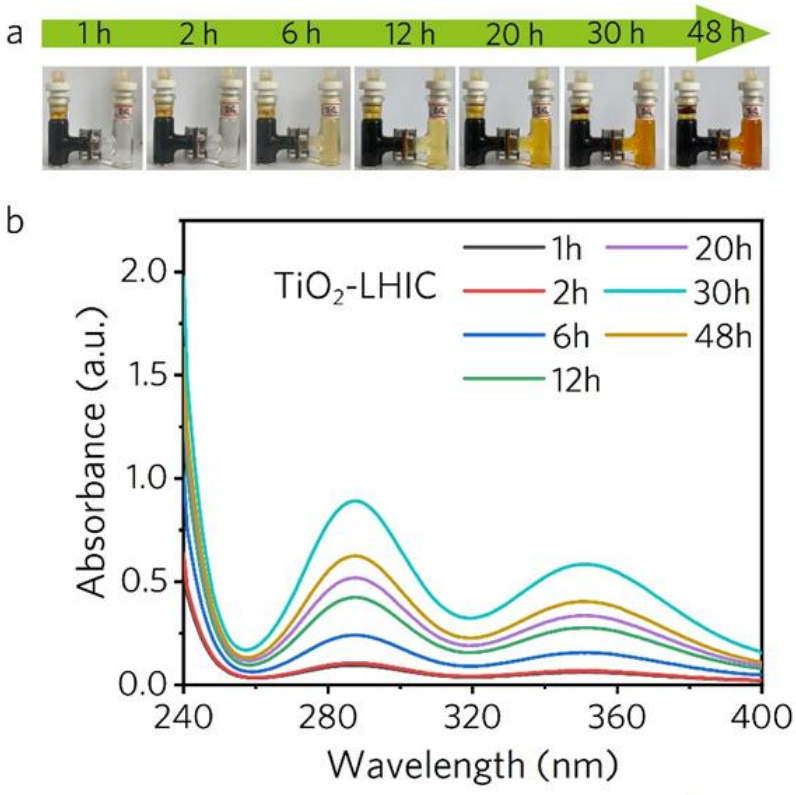

Figure S13. TiO_2-LHIC membrane penetration experiment in different durations: a) Optical photos and b) UV-vis results of the KI_x permeate side.

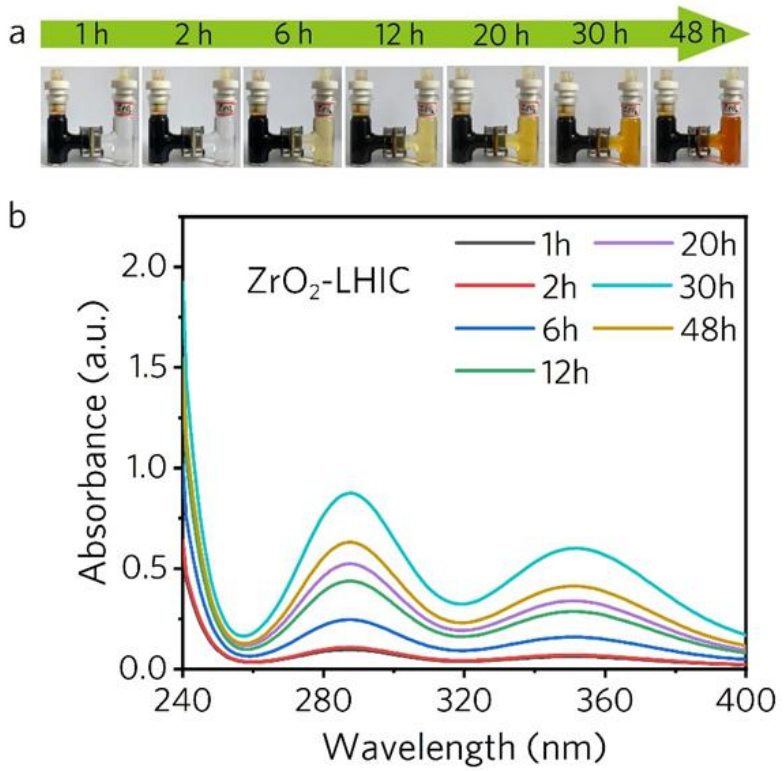

Figure S14. ZrO_2-LHIC membrane penetration experiment in different durations: a) Optical photos and b) UV-vis results of the KI_x permeate side.

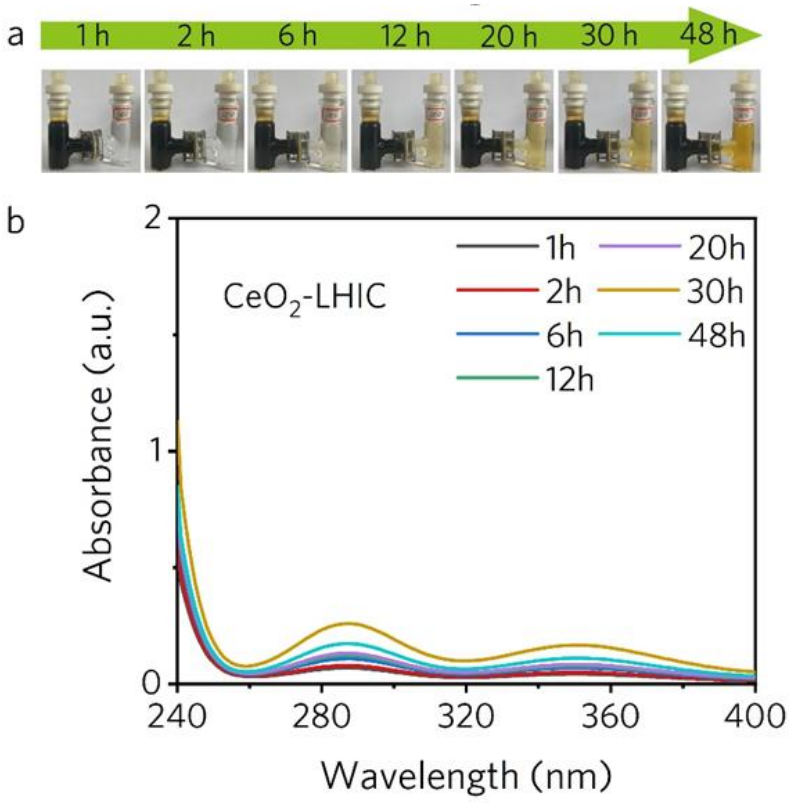

Figure S15. CeO_2-LHIC membrane penetration experiment in different durations: a) Optical photos and b) UV-vis results of the KI_x permeate side.

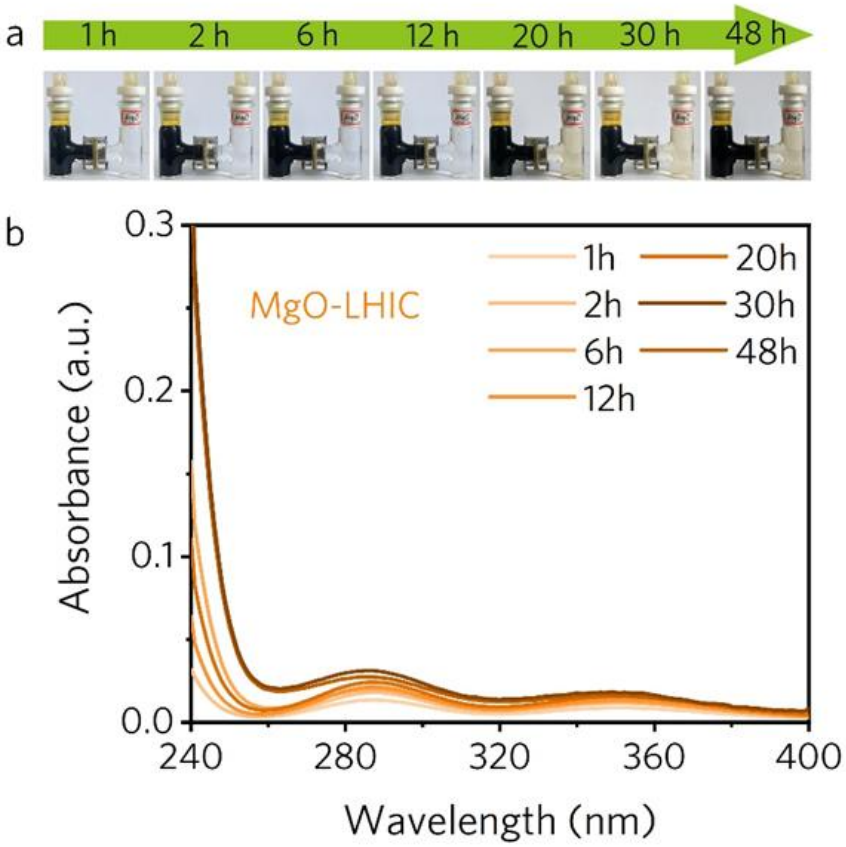

Figure S16. MgO-LHIC membrane penetration experiment in different durations: a) Optical photos and b) UV-vis results of the KI_x permeate side.

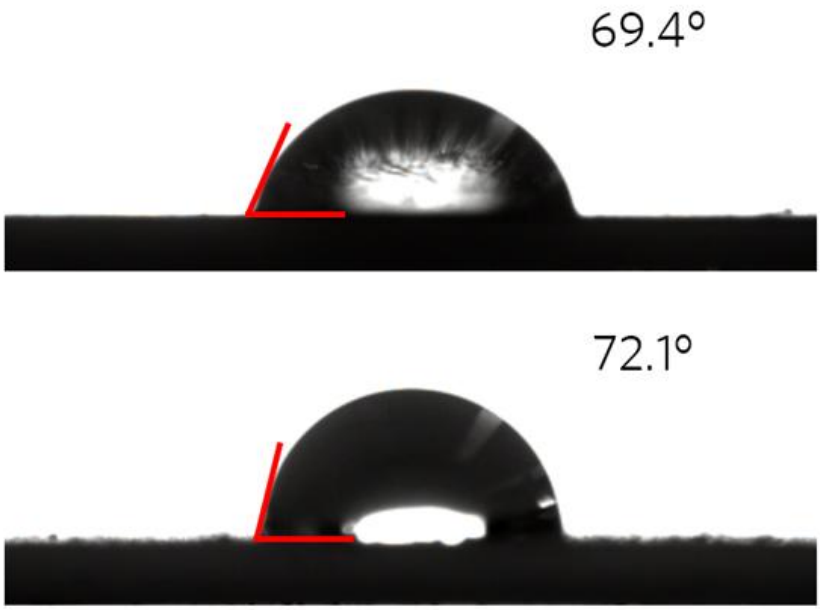

Figure S17. Comparison of contact angles between porous polyolefin membrane (69.4°) and MgO-LHIC composite membrane (72.1°).

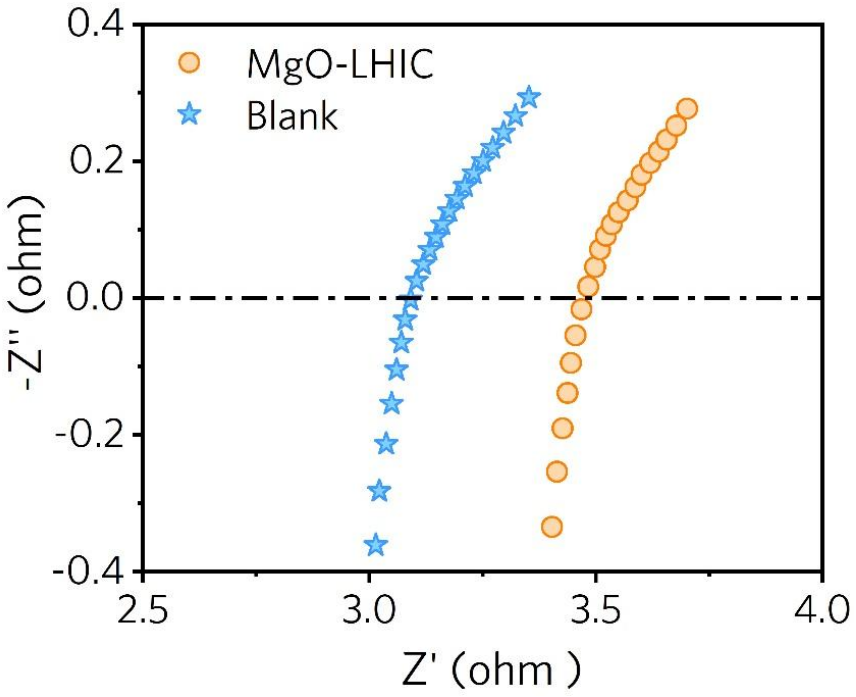

Figure S18. The EIS curves of ZIFBs with different membranes.

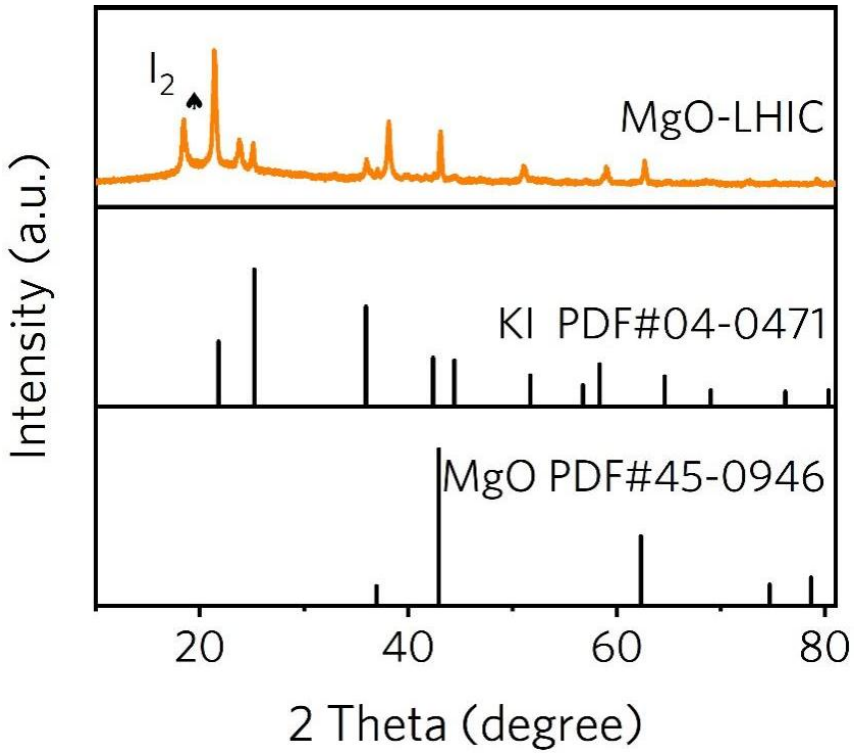

Figure S19. The XRD profile of the MgO-LHIC membrane.

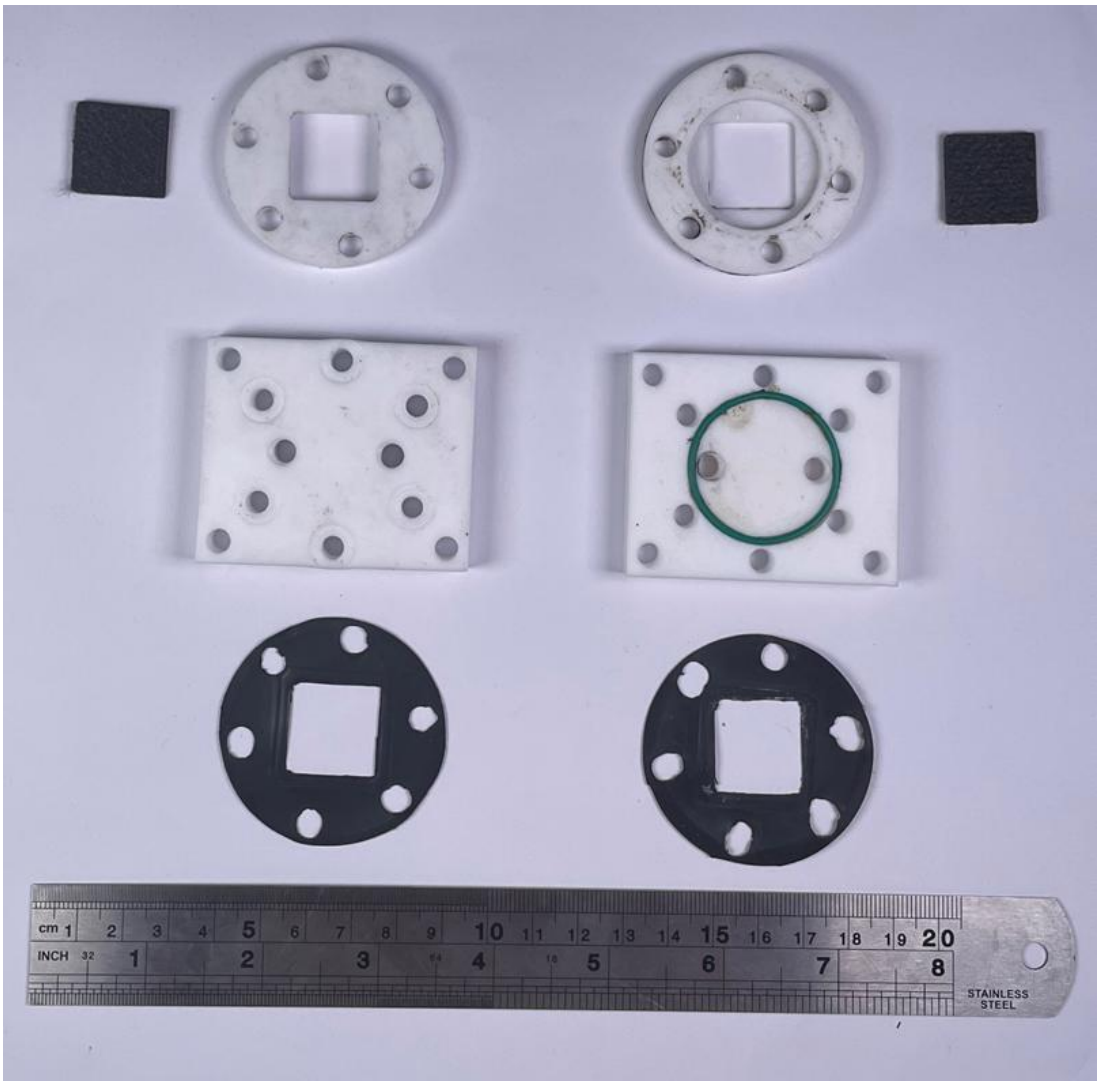

Figure S20. The optical image of the device components used in ZIFBs.

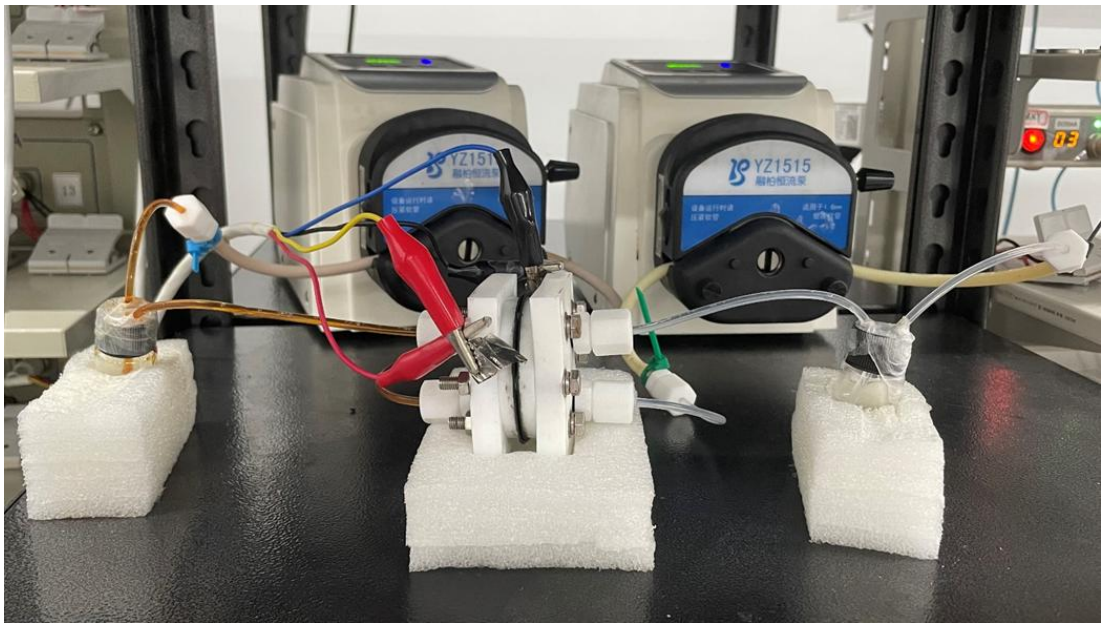

Figure S21. Operation optical image of ZIFBs at room temperature.

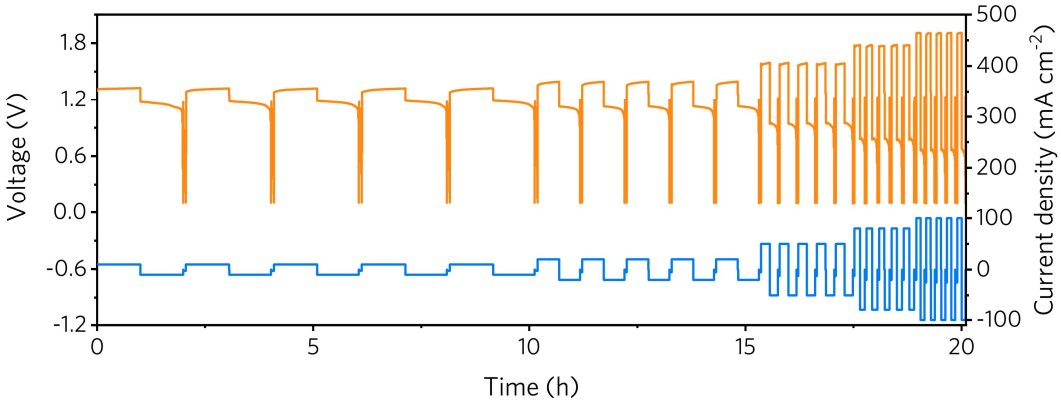

Figure S22. Galvanostatic cycling of MgO-LHIC membrane-based battery (4.5 ml of 1 M ZnI_2|| MgO-LHIC||4.5 ml of 1 M $ZnBr_2$, 4 cm^2 membrane area) under 10, 20, 50, 80 and 100 mA cm^{-2} at room temperature.

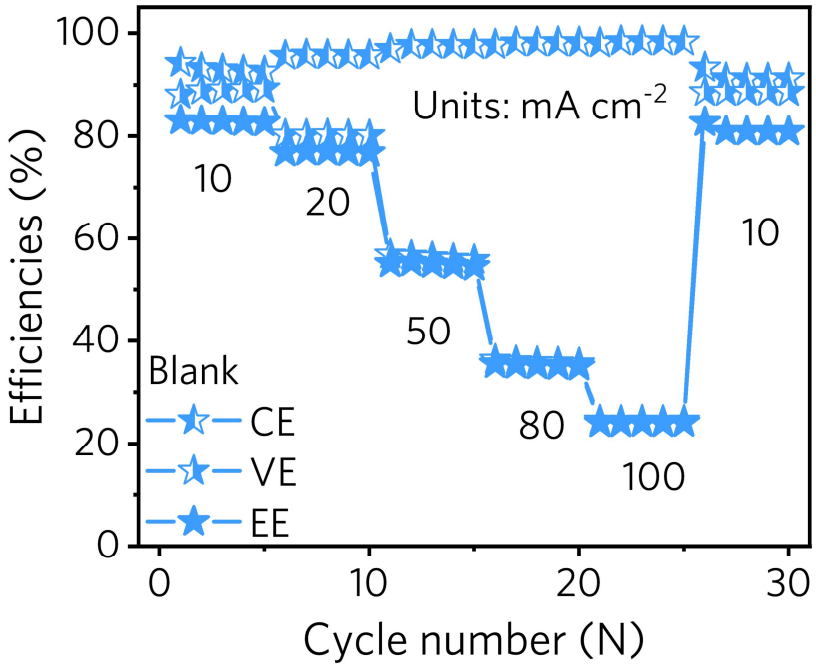

Figure S23. Efficiencies of blank porous polyolefin membrane at different currents.

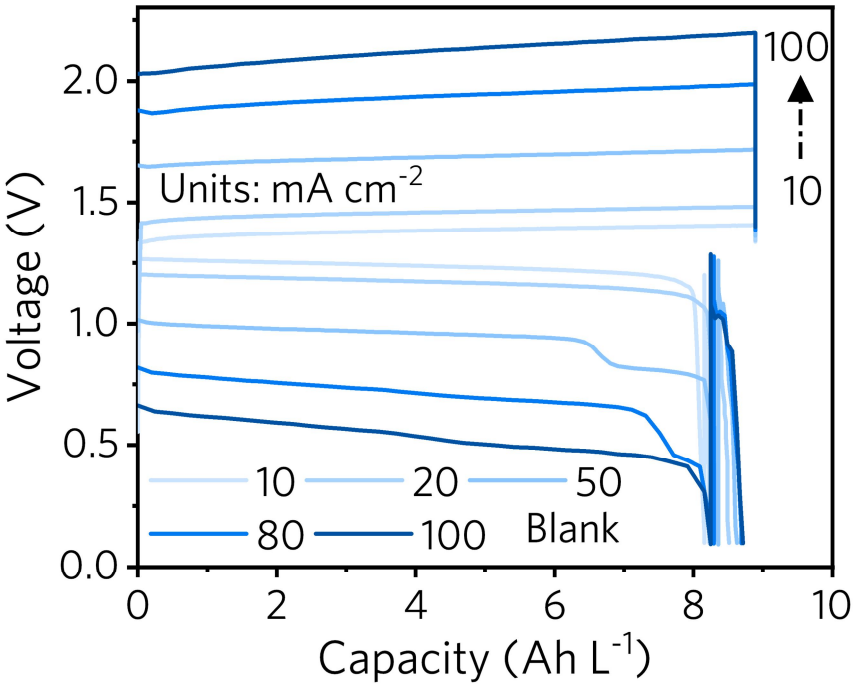

Figure S24. Voltage profiles of the ZIFBs using blank membrane under 10, 20, 50, 80, and 100 mA cm^{-2} at room temperature.

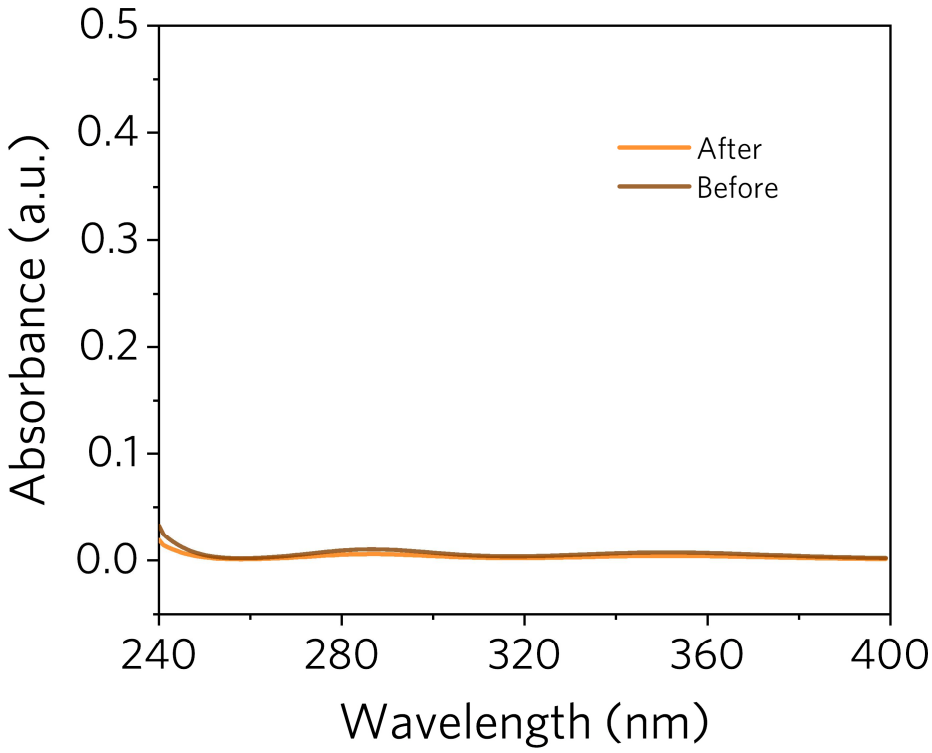

Figure S25. UV-vis results of the I_x^- in the anolyte before and after 50 cycles.

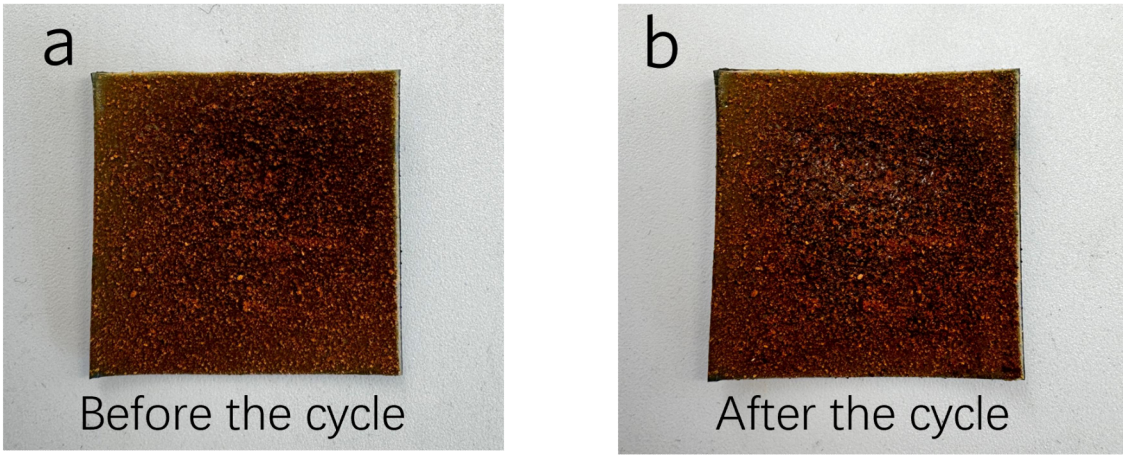

Figure S26. The morphology comparison of MgO-LHIC composite membrane before and after 50 cycles

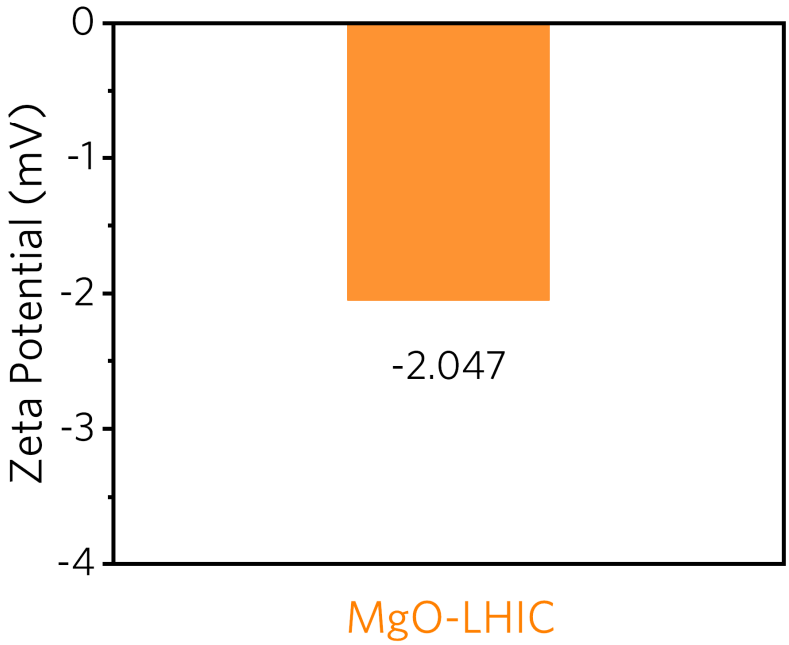

Figure S27. The Zeta potential of MgO-LHIC composite membrane after 50 cycles

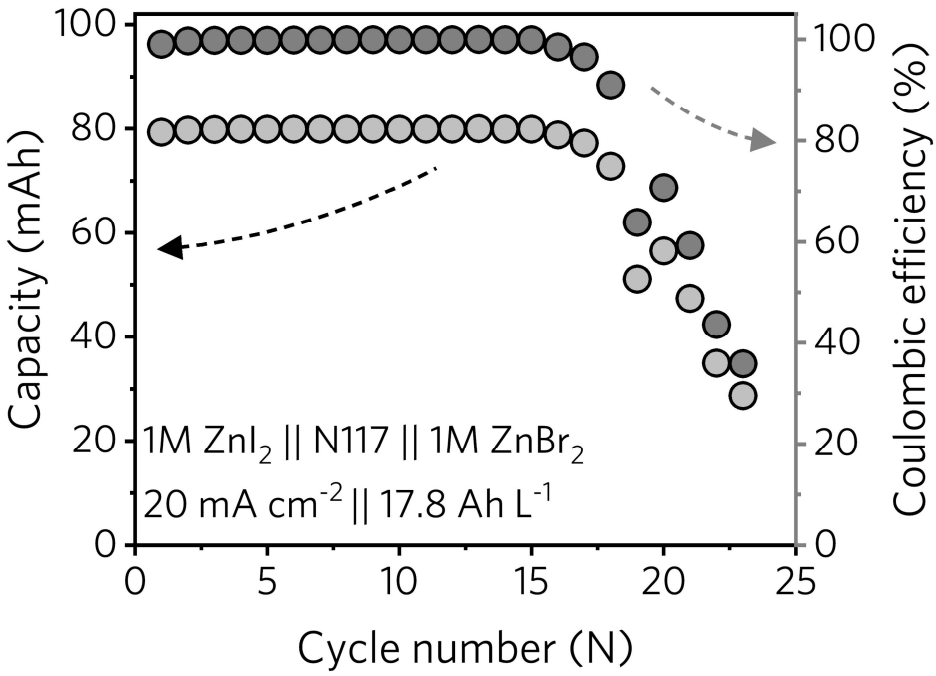

Figure S28. The cycle performance of the Nafion N117 membrane-based battery at 20 mA cm^{-2}.

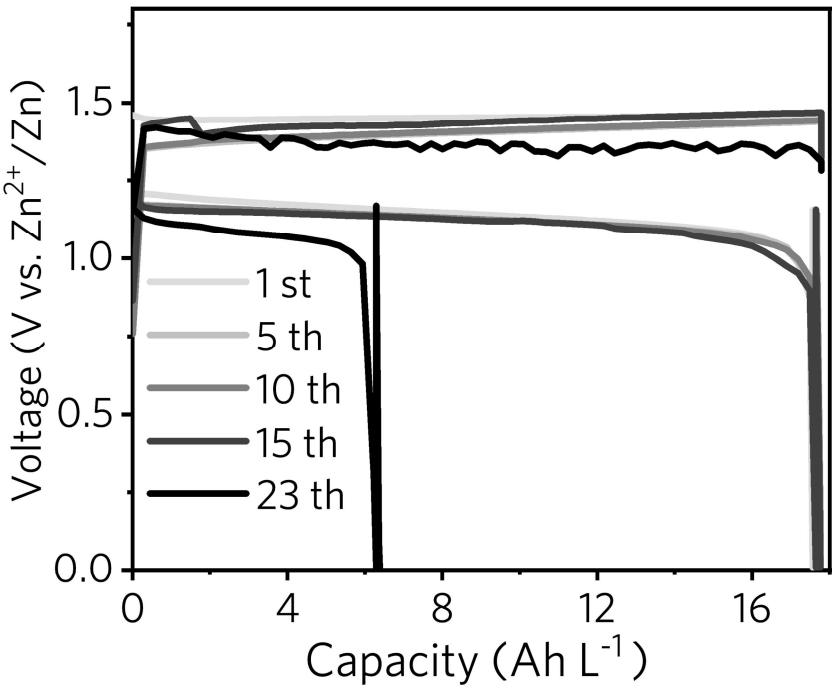

Figure S29. The cycle diagram of the Nafion N117 membrane-based battery at 20 mA cm^{-2} and the selected capacity-voltage curves 1 to 23 cycles.

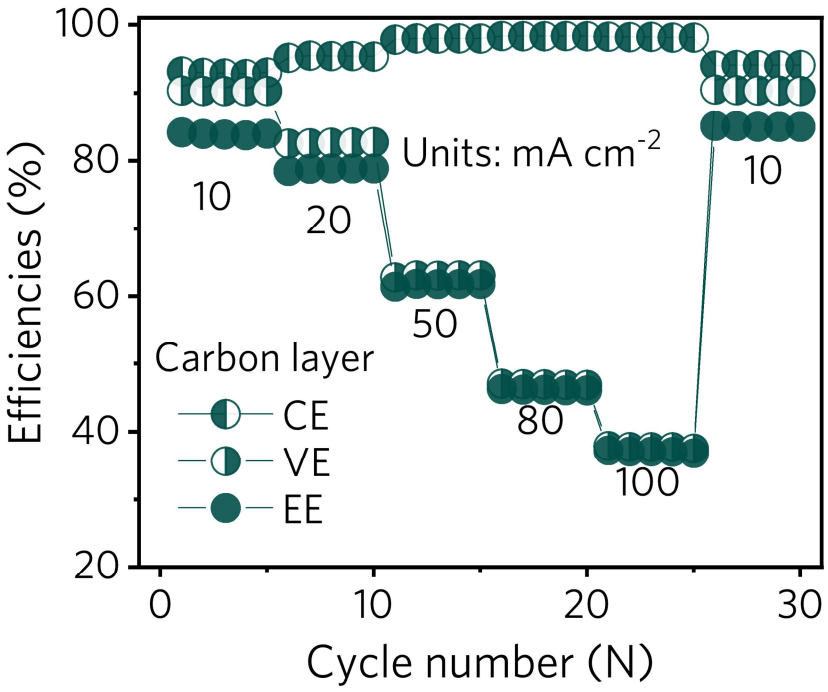

Figure S30. The cycle diagram of Carbon layer composite membrane-based battery at 20 mA cm^{-2} and the selected capacity-voltage curves 1 to 23 cycles.

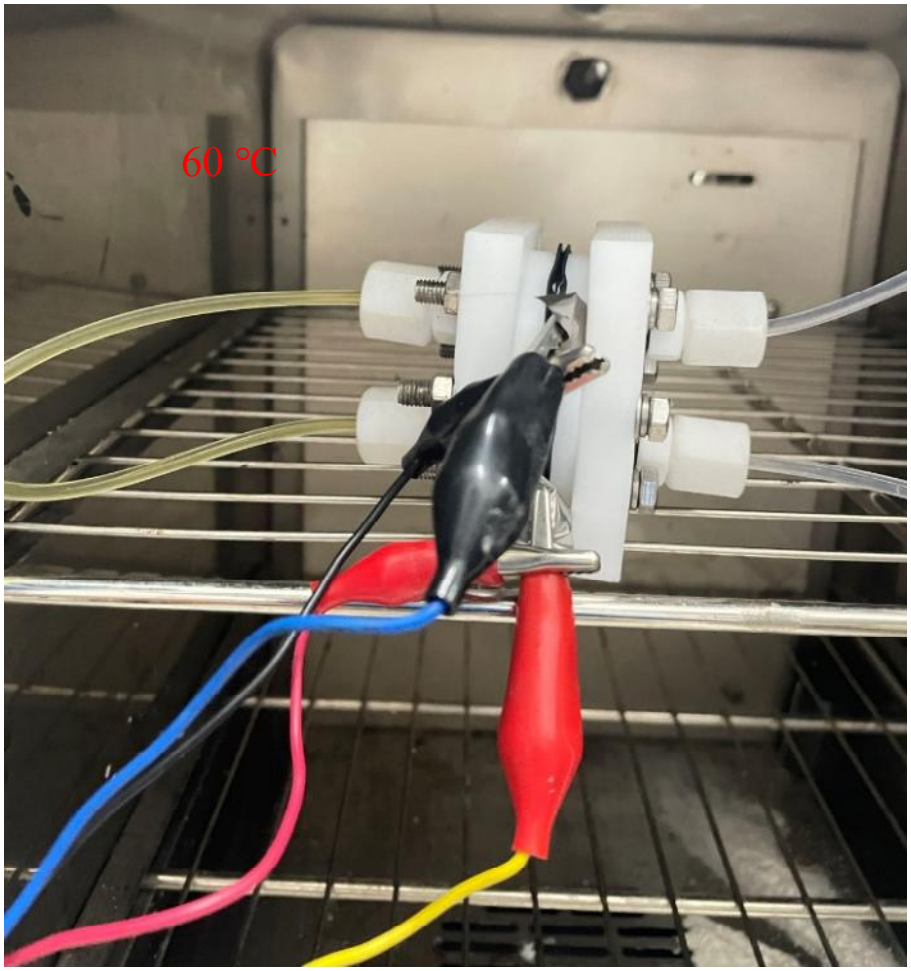

Figure S31. Operation diagram of ZIFBs using LHIC-based membrane at 60 °C.

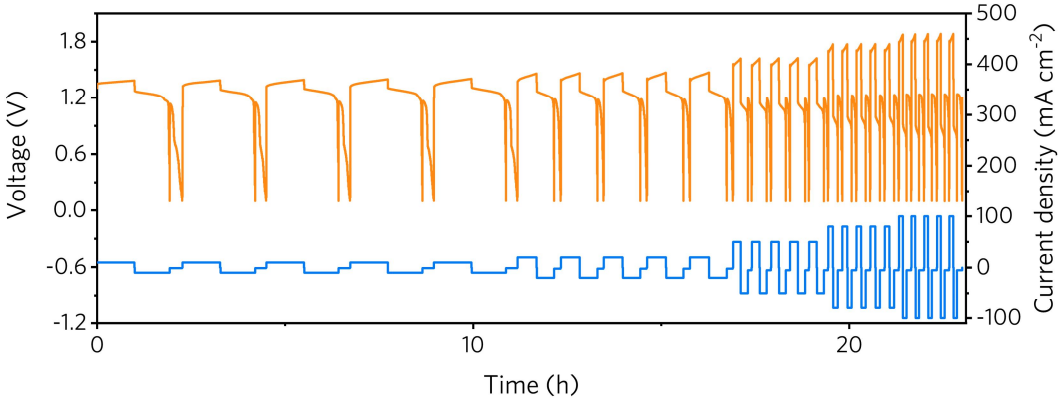

Figure S32. Galvanostatic cycling of MgO-LHIC membrane-based battery (4.5 ml of 1 M ZnI_2 || MgO-LHIC || 4.5 ml of 1 M $ZnBr_2$ +1 M KCl) under 10, 20, 50, 80 and 100 mA cm^{-2} at 60 °C.

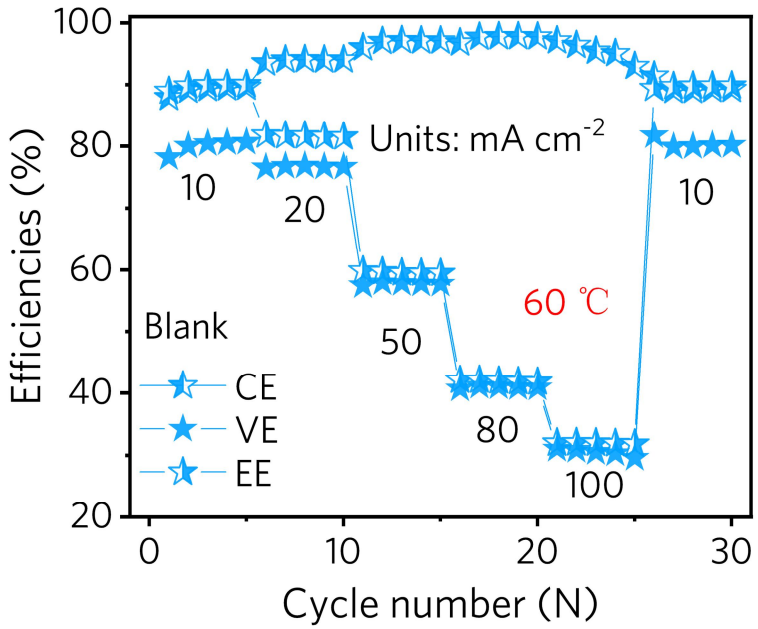

Figure S33. Efficiencies of porous polyolefin membrane-based battery at different working currents.

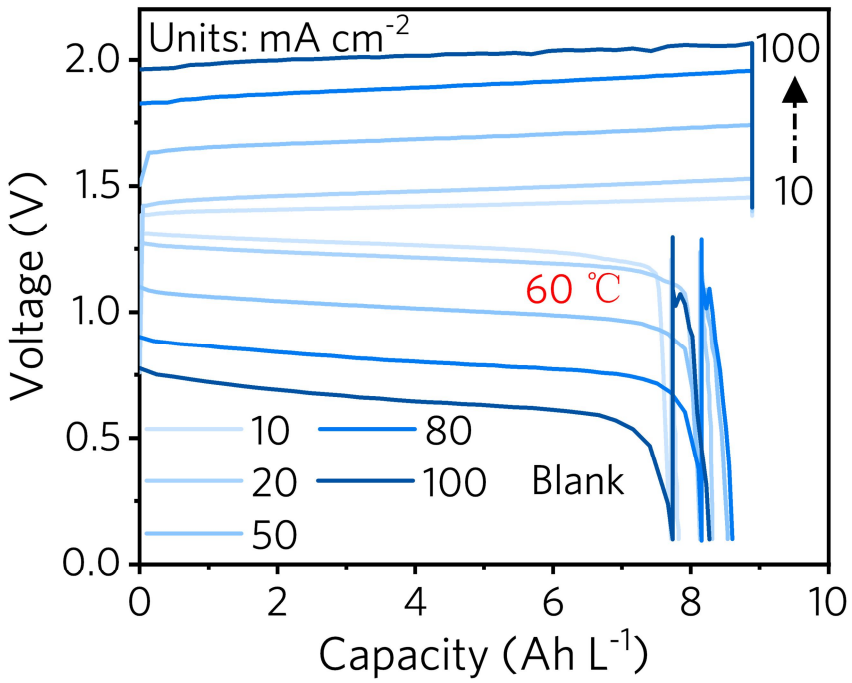

Figure S34. Voltage profiles of the ZIFBs using Blank membrane under 10, 20, 50, 80, and 100 mA cm^{-2} at 60 °C.

Reference

1 Z. Li, Y. C. Lu, *Nat. Energy*, 2021, **6**, 517.

2 X. Qiu, W. Li, S. Zhang, H. Liang, W. Zhu, *J. Electrochem. Soc.*, 2003, **150**, 917.

3 X. Li, S. Zhang, J. Du, L. Liu, C. Mao, J. Sun, A. Chen, *Nano Res.*, 2023, **16**, 9273.

4 Y. Guo, R. Zhang, S. Zhang, Y. Zhao, Q. Yang, Z. Huang, B. Dong, C. Zhi, *Energy Environ. Sci.*, 2021, **14**, 3938.